Zhang *et al. Energy Mater.* **2025**, *5*, 500023
DOI: 10.20517/energymater.2024.53

Energy Materials

Article

Open Access

Check for updates

Catalytic decomposition of methane: Ni-promoted perovskite oxide catalysts for turquoise hydrogen and carbon nanomaterials Co-production

Lan Zhang[1,2,#], Weike Zhang[1,#], Chee Kok Poh[3], Hongquan He[3], Qing Yue Kouk[3], Ovi Lian Ding[1,2], Lili Zhang[3,*], Siew Hwa Chan[1,2,*], Jiren Zeng[4], Guang Cao[5], Saifudin Abubakar[6]

[1]Energy Research Institute at NTU (ERI@N), Nanyang Technological University, Singapore 637141, Singapore.
[2]School of Mechanical and Aerospace Engineering, Nanyang Technological University, Singapore 639798, Singapore.
[3]Institute of Sustainability for Chemicals, Energy and Environment (ISCE[2]), Agency for Science, Technology and Research (A*STAR), Jurong Island 627833, Singapore.
[4]ExxonMobil Technology and Engineering, Shanghai Technology Center, Shanghai 200241, China.
[5]ExxonMobil Technology and Engineering, Annandale, NJ 08801, USA.
[6]ExxonMobil Technology and Engineering, Singapore 098633, Singapore.
[#]Authors contributed equally.

[*]**Correspondence to:** Prof. Siew Hwa Chan, School of Mechanical and Aerospace Engineering, Nanyang Technological University, 50 Nanyang Avenue, Singapore 639798, Singapore. E-mail: mshchan@ntu.edu.sg; Dr. Zhang Lili, Institute of Sustainability for Chemicals, Energy and Environment (ISCE2), Agency for Science, Technology and Research (A*STAR), 1 Pesek Road, Jurong Island 627833, Singapore. E-mail: zhang_lili@isce2.a-star.edu.sg

How to cite this article: Zhang, L.; Zhang, W.; Poh, C. K.; He, H.; Kouk, Q. Y.; Ding, O. L.; Zhang, L.; Chan, S. H.; Zeng, J.; Cao, G.; Abubakar, S. Catalytic decomposition of methane: Ni-promoted perovskite oxide catalysts for turquoise hydrogen and carbon nanomaterials Co-production. *Energy Mater.* **2025**, *5*, 500023. https://dx.doi.org/10.20517/energymater.2024.53

Received: 30 May 2024 **First Decision:** 23 Jul 2024 **Revised:** 6 Sep 2024 **Accepted:** 12 Oct 2024 **Published:** 15 Jan 2025

Academic Editor: Sining Yun **Copy Editor:** Ping Zhang **Production Editor:** Ping Zhang

Abstract

This study investigates the effectiveness of catalytic decomposition of methane for producing turquoise hydrogen and solid carbon nanomaterials. The focus is on developing cost-effective and high-performance Nickel (Ni)-promoted perovskite oxide catalysts. A series of transition metal, Ni-promoted $(La_{0.75}Ca_{0.25})(Cr_{0.5}Mn_{0.5})O_{3-\delta}$ (LCCM) catalysts have been successfully prepared using water-based gel-casting technology. These catalysts are designed to decompose methane into turquoise hydrogen and carbon nanomaterials, achieving negligible CO_2 emissions. X-ray diffraction results indicate that the solubility of Ni at the B-site of LCCM perovskite is limited, $x \leq 0.2$. Field Emission Scanning Electron Microscopy analysis of xNi-LCCM, calcined at 1050 °C for ten h in the air, confirms severe catalyst sintering with excess nickel oxide distributed around the LCCM particles. At a 750 °C operating temperature, a Ni to LCCM molar ratio of 1.5 yields a maximum carbon output of 17.04 g_C/g_{Ni}. Increasing the molar ratios to 2.0 and 2.5 results in carbon yields of 17.17 g_C/g_{Ni} and 17.63 g_C/g_{Ni}, respectively, showing minor changes.

The morphology of the carbon nanomaterials is unaffected by the molar ratio of NiO promoter to LCCM and remains nearly the same within the scope of this study.

Keywords: Methane decomposition, Ni-promoted perovskite oxide catalysts, turquoise hydrogen, carbon nanomaterials, metal exsolution

INTRODUCTION

Hydrogen (H_2), recognized as a sustainable alternative to fossil-based fuels, can be produced through various methods, each with distinct environmental impacts. These methods are categorized into seven types based on the processes and resources involved: White (Gold) Hydrogen, Green Hydrogen, Grey Hydrogen, Blue Hydrogen, Brown Hydrogen, Turquoise Hydrogen, and Pink Hydrogen, as illustrated in Figure 1[1-3]. Throughout the history of industrial chemistry, hydrogen has been one of the most important chemicals. According to the International Energy Agency (IEA), chemical and petrochemical applications account for over 95% of pure hydrogen consumption and 70% of the total hydrogen demand. Most of this hydrogen is used in ammonia synthesis, methanol production, and refining processes[4,5].

The use of microorganisms to generate bio-hydrogen represents a significant technological advancement, offering a renewable method for producing H_2 from biomass. Additionally, steam reforming, partial oxidation, and gasification are thermocatalytic processes commonly employed for hydrogen production[6]. Steam methane reforming (SMR) is a necessary industrial process for converting methane into grey or blue hydrogen, depending on whether carbon dioxide is captured[7-9]. SMR is a well-researched and mature technology[4,10-14]. Recently, Do *et al.* have introduced a new carbon-neutral hydrogen production method using electrified SMR (e-SMR) powered by renewable electricity, which extracts hydrogen from natural gas. Due to its ability to integrate hybrid primary energy inputs, utilize conventional natural gas as a feedstock, and employ both conventional and renewable energy for utilities, e-SMR is highly adaptable to the diverse energy landscapes of various countries[15]. Unlike the use of carbon capture and storage (CCS) technology for mitigating CO_2 emissions in the "blue hydrogen" production process, the concept of "turquoise hydrogen" involves converting natural gas (primarily CH_4) into hydrogen and value-added solid carbon nanomaterials, resulting in nearly zero emissions[16-18].

A literature review has been conducted to understand the conditions and effects of methane cracking reactions. Methane cracking is an endothermic process, thus requiring high temperatures. Temperatures above 1200 °C are necessary for the non-catalytic cracking of methane due to the stability of C-H bonds[19,20]. However, using a catalyst can significantly reduce the required temperature through pyrolysis reactions[21]. Catalysts, typically metal or metal oxide-based, are employed to promote methane cracking reactions, lowering reaction temperatures significantly and influencing the types and properties of carbon products[22]. Transition metals such as Ni (Nickel), Co (Cobalt), and Fe (Iron) are favored for their high catalytic activity and affordability[23]. The ranking of catalytic activity among transition metals is generally as follows: Co, Ru, Ni, Rh > Pt, Re, Ir > Pd, Cu, W, Fe, Mo[19]. Different catalysts have pros and cons based on the literature review conducted, and it was found that catalyst supports also affect catalytic performance.

The deactivation of catalysts remains a major hurdle in methane catalytic cracking. Therefore, selecting an optimum operating temperature that balances carbon formation and diffusion rates is necessary to extend the catalyst lifetime while maintaining the required catalytic activity[16,24-27]. While most catalysts adhere to the tip growth mechanism during the Catalytic Decomposition of Methane (CDM) reaction, exceptions exist. In cases where the interaction between active catalyst and substrate phases is strong enough, the "base

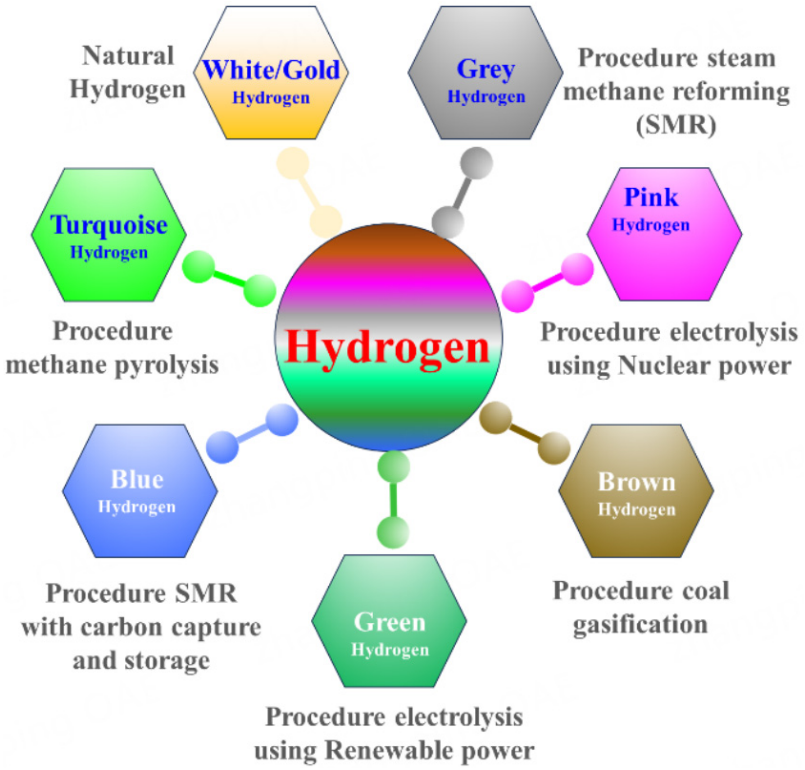

Figure 1. Classification of hydrogen production into seven types based on process and resource involvement.

growth" mechanism occurs, resulting in carbon filaments growing from the metal-gas interface[2].

Compared to Ni-supported catalysts, perovskite catalysts can withstand higher temperatures, resulting in a higher methane conversion rate. For instance, the $LaNiO_3$ catalyst for methane deposition to produce carbon nanotubes and CO_x-free hydrogen has been tested at temperatures ranging from 600 to 800 °C[26,28]. However, $LaNiO_3$ decomposed after pre-reduction with pure hydrogen at 700 °C in one hour, indicating that Ni loaded on La_2O_3 support will not prevent Ni sintering under operating conditions.

The perovskite structure, with the composition $(La_{0.75}A_{0.25})(Cr_{0.5}Mn_{0.5})O_{3-\delta}$ [where A=Ca for $(La_{0.75}Ca_{0.25})(Cr_{0.5}Mn_{0.5})O_{3-\delta}$ (LCCM) and A=Sr for $(La_{0.75}Sr_{0.25})(Cr_{0.5}Mn_{0.5})O_{3-\delta}$ (LSCM)], has been widely adopted in high-temperature solid oxide fuel cell (SOFC) materials due to its redox properties[29-33]. Jiang et al. reported that the conversion of methane in LSCM was low[29], and the dry reforming of methane over Gd-doped ceria (GDC)-impregnated LSCM electrodes was better than that of LSCM and LSCM/yttria-stabilized zirconia (YSZ) electrodes[30]. The substitution of perovskite A-sites with Ca, Sr, and B-sites with Mg, Mn, Fe, Co, and Ni for the SOFC anode material has been found to enhance catalyst activity towards carbon deposition situation[31,32]. Li *et al.* reported that transition metal nanoparticle was grown on the LSCM electrode surface via *in-situ* exsolution of transition metal from A-site deficient and B-site excess[34]. Sun *et al.* reported that Fe and Cu co-dopped in B-site of LSCM exhibited higher catalytic activity, with CO productivity of up to 4.41 mL min^{-1} cm^{-2} at 1.6 V and 850 °C, in contrast to its CO yield which was 2.6 times that of the undoped LSCM[35]. Jardiel *et al.* reported that the solid solution limit was 20% nickel on the B-site of $(La_{0.75}Sr_{0.25})(Cr_{0.5}Mn_{0.5-x}Ni_x)O_{3-\delta}$ and $(La_{0.75}Sr_{0.25})(Cr_{0.5-x}Ni_xMn_{0.5})O_{3-\delta}$[36]. Furthermore, Carrillo *et al.* summarized new trends in nanoparticle exsolution and reported that nanoparticle exsolved could control the shape and the number of elements[37]. In this paper, we propose synthesizing a Ni-promoted LCCM catalyst for methane cracking,

with the expectation that Ni will be exsolved from the B-site of LCCM to enhance the catalytic performance of the catalyst.

The cost of the catalyst is another significant challenge hindering commercialization. Using carbonates and oxides as raw materials and synthesizing via a solid-state reaction can lower the cost, but the performance will be penalized. The materials synthesized through the gel-casting method exhibit lower phase formation temperatures, narrower particle size distributions, improved sintering properties, and enhanced electrochemical activity[38-40]. For example, the phase formation temperature of LSCM has been reduced by over 100 °C[33,38], and the sintering temperature of apatite electrolytes has been lowered by more than 200 °C[40]. A significant advantage of powders synthesized via the gel-casting process is their ability to be mass-produced at a low cost.

Therefore, this paper investigates the enhancement of catalytic activity of LCCM through Ni over-doping, synthesized in one step via the gel-casting technique at different molar ratios, for methane catalytic cracking. This catalyst is expected to possess reactivity, and low production costs, making it easily scalable for mass production.

EXPERIMENTAL

Preparation of Ni-Promoted LCCM

The LCCM oxide promoted by NiO catalysts (*x*Ni-LCCM) was synthesized using a water-based gel-casting method. Samples were denoted based on their Ni to LCCM molar ratios; for the sample, a ratio of 0 mol Ni resulted in the designation 00Ni-LCCM. When the molar ratio was 0.5 mol, the sample was denoted as 05Ni-LCCM. All designated columns are listed in Table 1. For instance, in the 15Ni-LCCM synthesis, the following quantities were used: La_2O_3 (45.82 g), $CaCO_3$ (9.38 g), Cr_2O_3 (14.25 g), $MnCO_3$ (21.55 g), NiO (42.01 g). These were homogeneously mixed with a dispersant solution containing 6.65 g of a 30 wt.% ammonium polymethacrylate (PMAA) solution, 0.67 g polyvinylpyrrolidone (PVP K30), and 27.21 g of a 2 wt.% N,N,N',N'-Tetramethyl ethylenediamine (TEMED) solution, along with 108.83 g of distilled water. The mixture was milled for one hour and 45 mins at 150 rpm in a Retsch planetary ball mill machine (PM 100), using zirconia milling jars and zirconia balls. Subsequently, 27.21 g of acrylamide (AM, $C_2H_3CONH_2$) and 1.81 g of *N,N'*-methylenebisacrylamide (MBAM, $C_2H_3CONHCH_2NHCOC_2H_3$) were added for an additional 15 mins of planetary ball milling. The AM to MBAM weight ratio was 15:1. Finally, 27.21 g of a 2 wt.% solution of ammonium persulfate [APS, $(NH_4)_2S_2O_8$] was added as an initiator. The resulting slurry was then poured into a covered beaker and placed in an oven maintained at 80 °C for 45 mins. The gel-casting procedures used to prepare the xNi-LCCM series powders in this article are nearly the same as those used to synthesize LSCM powders reported in the published paper[33,39]. Figure 2 illustrates the modified catalyst procedure synthesized through the water-based gel-casting process in one step without premixing. This improved process does not use organic solvents, and the ball grinding time is considerably shortened, significantly reducing production costs. The resulting precursors were then cut, dried, and calcined at 1050 °C for ten h in a high-temperature box furnace to form the *x*Ni-LCCM catalysts. All the raw materials purchased from Sigma-Aldrich were used without any further purification treatment.

Characterization and catalytic performance measurements

The phase of the as-prepared powders was determined by X-ray diffraction (XRD) using $CuK_{\alpha 1}$ radiation (l = 1.54060 Å) at room temperature. X-ray scans were conducted over a 2θ spectrum ranging from 20° to 80° at a scan rate of 4° min^{-1}. The thermal behavior of the precursors and produced carbon nanomaterials were analyzed using a Thermogravimetric Analyzer (TGA) Q500 thermal analyzer (TA Instruments) with a heating rate of 5 °C min^{-1} under an airflow of 100 mL min^{-1}. Field Emission Scanning Electron Microscopy

Table 1. Molar ratios and denoted names of Ni-promoted LCCM series catalysts

S/N	Molar ratio	Denoted as
#1	$Ni_{0.0}$:$La_{0.75}Ca_{0.25}Cr_{0.5}Mn_{0.5}O_{3-\delta}$ = 0:1	00Ni-LCCM
#2	$Ni_{0.2}$:$La_{0.75}Ca_{0.25}Cr_{0.5}Mn_{0.5}O_{3-\delta}$ = 0.2:1	02Ni-LCCM
#3	$Ni_{0.5}$:$La_{0.75}Ca_{0.25}Cr_{0.5}Mn_{0.5}O_{3-\delta}$ = 0.5:1	05Ni-LCCM
#4	$Ni_{1.0}$:$La_{0.75}Ca_{0.25}Cr_{0.5}Mn_{0.5}O_{3-\delta}$ = 1.0:1	10Ni-LCCM
#5	$Ni_{1.5}$:$La_{0.75}Ca_{0.25}Cr_{0.5}Mn_{0.5}O_{3-\delta}$ = 1.5:1	15Ni-LCCM
#6	$Ni_{2.0}$:$La_{0.75}Ca_{0.25}Cr_{0.5}Mn_{0.5}O_{3-\delta}$ = 2.0:1	20Ni-LCCM
#7	$Ni_{2.5}$:$La_{0.75}Ca_{0.25}Cr_{0.5}Mn_{0.5}O_{3-\delta}$ = 2.5:1	25Ni-LCCM

LCCM: $(La_{0.75}Ca_{0.25})(Cr_{0.5}Mn_{0.5})O_{3-\delta}$.

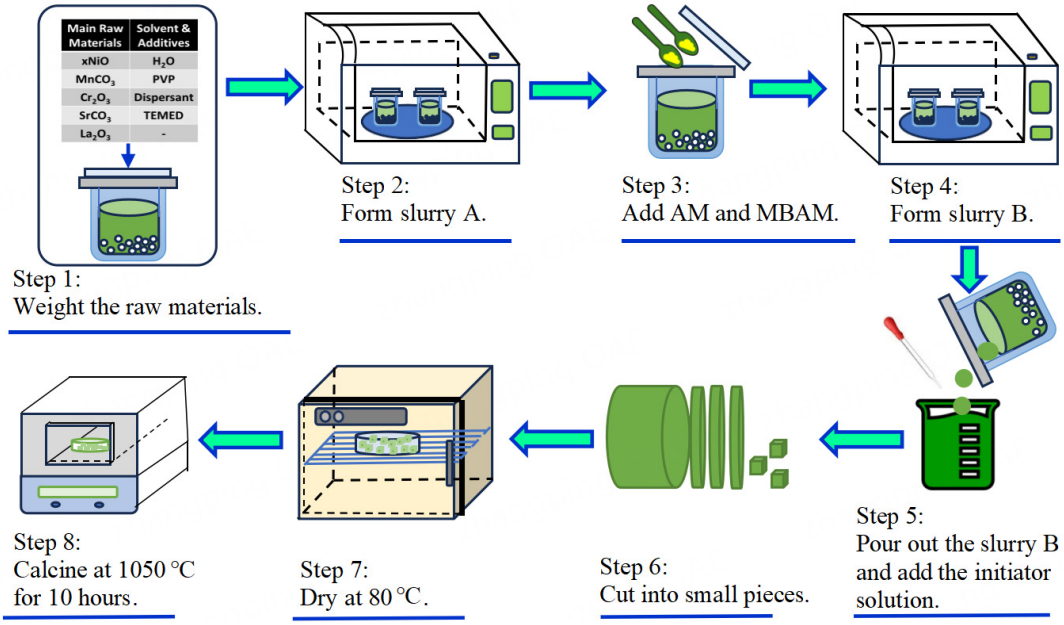

Figure 2. Flow chart of synthesis process for xNi-LCCM series catalysts using water-based gel-casting. LCCM: $(La_{0.75}Ca_{0.25})(Cr_{0.5}Mn_{0.5})O_{3-\delta}$; MBAM: *N,N'*-methylenebisacrylamide; AM: Acrylamide.

(FESEM, JEOL JSM-7600F) was employed to investigate the morphology of the as-produced carbon nanomaterials.

Methane decomposition experimental setup

The schematic illustrations of the experimental setup used to assess the stability of xNi-LCCM under reducing atmospheric conditions and methane decomposition reactions at different temperatures are shown in Figure 3. The fixed-bed thermal reactor is constructed from a quartz tube with a length of 120 cm, an outer diameter of 23 mm, and an inner diameter of 18 mm. The reactor is heated using a single-zone resistive electrical heating system. The catalyst was loaded into the middle of the reactor tube. CH_4, N_2, and H_2 were introduced into the reactor using mass flow controllers to regulate the feed gas flow rate. When investigating the stability of xNi-LCCM catalysts under reducing atmospheres, the mixed gas stream comprised 20 standard cubic centimeter (SCCM) of H_2 and 30 SCCM of N_2. When studying methane decomposition reactions, the flow rate of CH_4 was maintained at 10 SCCM over a 0.2 g sample, resulting in a gas hourly space velocity (GHSV) of 3 $L{\cdot}g_{cat.}^{-1}{\cdot}h^{-1}$. The product gases were continuously analyzed using a gas chromatograph (GC-2030N-0402 Pro. SHIMADZU Japan) equipped with a thermal conductivity

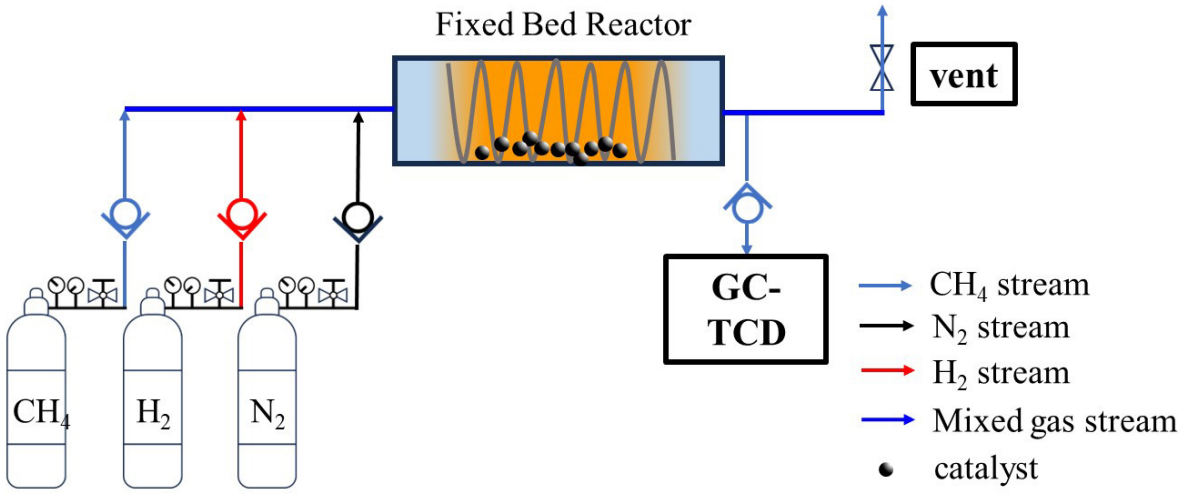

Figure 3. Schematic illustration of methane decomposition experimental setup.

detector column to determine the amounts of product gases, namely, H_2 and CH_4.

RESULTS AND DISCUSSION

Thermal analysis of precursor

Figure 4 shows the decomposition characteristics of the xNi-LCCM precursors observed in the TGA of the water-based gel-casting process. Below 250 °C, there were losses of approximately 2.5 wt.%, likely due to the endothermic removal of residual water in the polymer network and powder mixtures. The significant decomposition of the gel-casting precursors occurred within the temperature range of 250-450 °C, indicated by a sharp endothermic peak in the Differential Thermal Gravimetry (DTG) spectra around 375 °C. The decomposition suggests the thermal oxidation of the polymer network, the removal of bound molecular water, and the decomposition of carbonaceous precursors. The high-temperature decomposition characteristics of the xNi-LCCM gels result from the decomposition of $CaCO_3$. Due to the limitation of the TGA testing temperature range, the experiments could only be conducted up to a temperature of 950 °C. Based on published journal papers, the calcination temperature for xNi-LCCM was set at 1050 °C for ten h[38].

Phase of xNi-LCCM under reducing and CH_4 atmosphere

Figure 5 depicts the XRD patterns of the xNi-LCCM powder synthesized using water-based gel-casting techniques and treated under various temperatures and atmospheres. The powders underwent calcination at 1050 °C for ten h in the air, followed by treatment at 750 °C for two h under an H_2/N_2 gas blend in a tube furnace, and finally processed under CH_4 at 750 °C for 15 h in a fixed bed reactor, as shown in Figure 3. The phases of NiO, LCCM, Ni, and the produced carbon material are differentiated and indicated by various solid symbols: green triangle, brown square, grey triangle, and black circle, respectively.

Figure 5A illustrates the 00Ni-LCCM synthesized through a water-based gel-casting method and subsequently calcined at 1050 °C for ten h in the air. The XRD analysis confirmed the formation of the LCCM perovskite structure, aligning with previous research by Zhang *et al.* The XRD pattern of the synthesized LCCM powder matched that in the database, confirming successful perovskite structure formation[39]. As shown in Figure 5A, regarding the XRD pattern of 02Ni-LCCM, no second phase was detected when the ratio of Ni to LCCM was 0.2, indicating that all the incorporated nickel oxide entered the crystal structure of LCCM during the calcination process. Upon increasing the Ni content further, the XRD

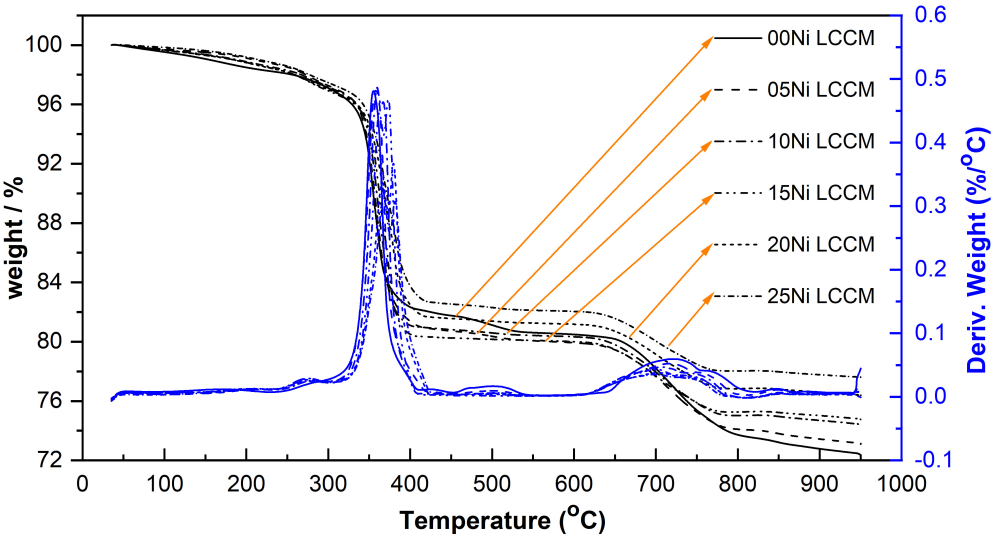

Figure 4. Decomposition characteristics of xNi-LCCM precursors prepared via water-based gel-casting, as analyzed by TGA. LCCM: $(La_{0.75}Ca_{0.25})(Cr_{0.5}Mn_{0.5})O_{3-\delta}$; TGA: A thermogravimetric analyzer.

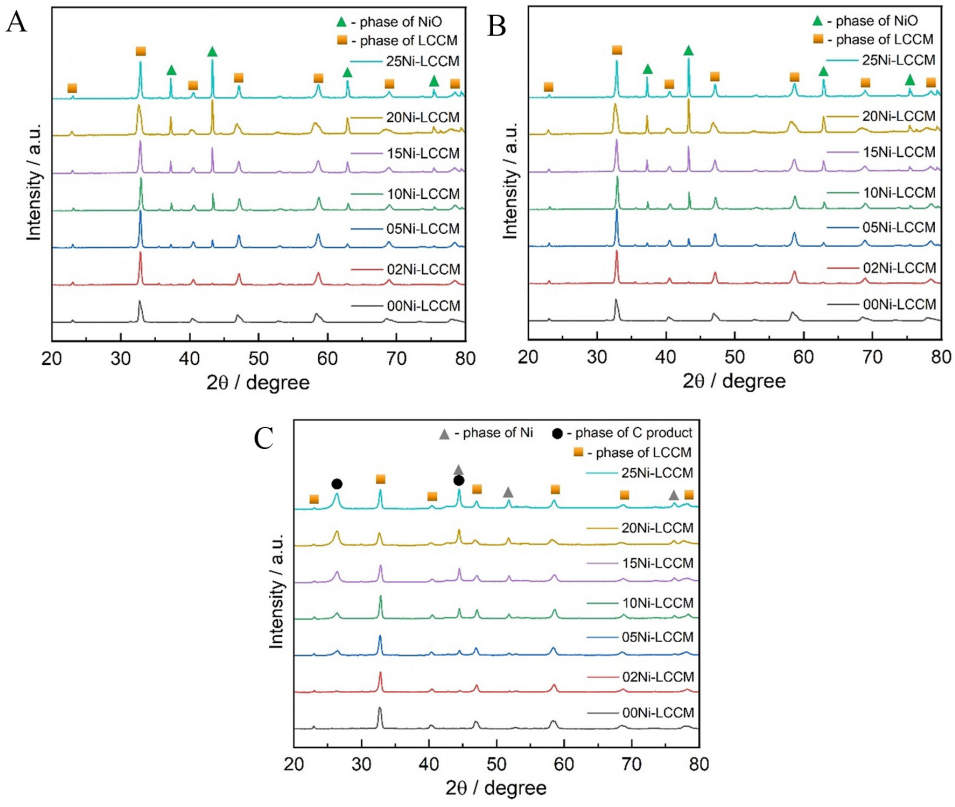

Figure 5. X-ray diffraction (XRD) patterns of the xNi-LCCM powder, synthesized using water-based gel-casting techniques, (A) calcined at 1050 °C for 10 h in air; (B) reduced at 750 °C for 2 h in N_2 blended H_2; (C) treated at 750 °C for 15 h in CH_4. The phases of LCCM, Ni, NiO, and the produced carbon material were differentiated and indicated by various solid symbols: brown square, grey triangle, green triangle, and black circle, respectively. LCCM: $(La_{0.75}Ca_{0.25})(Cr_{0.5}Mn_{0.5})O_{3-\delta}$.

patterns reveal the presence of nickel oxide phases, clearly due to the solubility limit of nickel oxide. This

phenomenon aligns with the findings by Jardiel *et al.*, who reported that the solid solution limit was 20 mol.% nickel on the B-site of LSCM[36].

As shown in Figure 5B, the XRD pattern of 00Ni-LCCM treated in a reducing atmosphere matched the XRD pattern of 00Ni-LCCM calcined in static air, indicating the stability of 00Ni-LCCM powders in a reducing environment. In the XRD pattern of 02Ni-LCCM treated in a reducing atmosphere, a peak of the Ni phase was detected, which is due to the exsolution of Ni metal from the crystal structure of 02Ni-LCCM. Li *et al.* reported that catalytically active copper nanoparticles are grown on the surface of the LSCM cathode via *in-situ* exsolution of copper metal from an A-site deficient and B-site excess after reduction[34]. As the nickel oxide content in the samples rises, the intensity of the nickel diffraction peaks significantly increases. This further supports the notion that the solubility of metallic nickel in the B-site of LCCM is limited.

As shown in Figure 5C, the XRD pattern of 00Ni-LCCM treated in a methane atmosphere is consistent with the XRD pattern of 00Ni-LCCM calcined in static air and treated in a reducing atmosphere, indicating that LCCM alone does not exhibit catalytic activity for methane cracking. Lanthanum chromite-based materials have been frequently reported for the direct oxidation of methane on SOFC anodes, noted for their high resistance to carbon deposition[29,31].

Peaks of carbon material were detected in the XRD patterns of all samples except for the 00Ni-LCCM sample. The diffraction reflection at approximately 26.4° can be attributed to graphite, while the reflection at around 44.5° results from the overlapping peaks of C and Ni, as indicated in Joint Committee on Powder Diffraction Standards (JCPDS) cards No. 96-101-1061 and No. 96-901-1598. However, a notable difference is the increased intensity of carbon and nickel peaks correlating with the rise in nickel concentration.

Furthermore, according to Figure 5B and C, the perovskite crystal structure of LCCM remains intact and has not decomposed into lanthanum oxide, calcium oxide, and metallic chromium and manganese. This is different from other perovskites, such as $LaNiO_3$, which decompose when used as catalyst precursors[26,28,41,42].

Weight change of xNi-LCCM under various atmospheres

Based on the XRD analysis results mentioned above, the amount of nickel doping at the B-site is limited, approximately 0.2 mol. The theoretical weight content of nickel in the different samples is calculated by

$$N_{xNi-LCCM} = \frac{W_{02Ni-LCCM} * N_{0.2Ni-LCCM} + W_{Ni-NiO}}{W_{02Ni-LCCM} + W_{NiO}} * 100\% \quad (1)$$

Where $N_{xNi\text{-}LCCM}$ represents the specific theoretical Ni weight percentage in the xNi-LCCM sample. $W_{02Ni\text{-}LCCM}$ refers to the Ni weight of $(La_{0.75}Ca_{0.25})(Cr_{0.5}Mn_{0.5}Ni_{0.2})O_{3-\delta}$ and $W_{Ni\text{-}NiO}$ is the Ni weight of NiO. The specific theoretical Ni weight percentages for different samples are listed in Table 2.

To assess the stability of xNi-LCCM under reducing atmospheric conditions, samples from the xNi-LCCM series were treated in a reducing atmosphere at 750 °C for 2h. The experimental weight loss percentage in the reducing atmosphere was calculated based on the weights of the samples before and after the treatment, as given in

$$W_L = -\frac{W_{RA} - W_{RB}}{W_{RB}} * 100\% \quad (2)$$

Table 2. Weight of xNi-LCCM under various atmospheres and carbon yields

Sample	N_{Ni}	W_L (H_2 + N_2)	750 °C for 15 h (CH_4)		800 °C for 15 h (CH_4)		850 °C for15 h (CH_4)	
			$Y_{C\ xNi\text{-}LCCM}$	$Y_{C\ Ni}$	$Y_{C\ xNi\text{-}LCCM}$	$Y_{C\ Ni}$	$Y_{C\ xNi\text{-}LCCM}$	$Y_{C\ Ni}$
	wt.%	wt.%	$g_C/g_{xNi\text{-}LCCM}$	g_C/g_{Ni}	$g_C/g_{xNi\text{-}LCCM}$	g_C/g_{Ni}	$g_C/g_{xNi\text{-}LCCM}$	g_C/g_{Ni}
00Ni-LCCM	0.00	-0.63	0.00	0.00	0.00	0.00	0.00	0.00
02Ni-LCCM	5.16	-1.92	0.32	6.20	0.33	6.40	0.35	6.78
05Ni-LCCM	11.75	-3.62	1.23	10.47	1.12	9.53	0.9	7.66
10Ni-LCCM	20.44	-5.99	2.92	14.29	2.37	11.59	2.33	11.40
15Ni-LCCM	25.94	-7.76	4.42	17.04	3.50	13.49	2.72	10.49
20Ni-LCCM	32.44	-9.14	5.57	17.17	4.35	13.41	3.38	10.42
25Ni-LCCM	36.76	-10.31	6.48	17.63	5.09	13.85	4.09	11.13

LCCM: $(La_{0.75}Ca_{0.25})(Cr_{0.5}Mn_{0.5})O_{3-\delta}$.

Where W_L represents the experimental weight loss percentage, W_{RB} denotes the sample's weight before undergoing reduction treatment, and W_{RA} corresponds to the sample's weight after reduction treatment.

The specific yield of carbon ($g_C/g_{xNi\text{-}LCCM}$) is calculated as follows:

$$Y_{C\text{-}xNi-LCCM} = \frac{m_{C\text{-}xNi-LCCM} - \frac{(100 + W_L) * m_{xNi-LCCM}}{100}}{m_{xNi-LCCM}} \quad (3)$$

Where $m_{C\text{-}xNi\text{-}LCCM}$ is the weight of carbon formed over the sample, including the sample weight (g); $m_{xNi\text{-}LCCM}$ is the weight of the sample (g).

The specific yield of carbon (g_C/g_{Ni}) is calculated as

$$Y_{C\text{-}Ni} = \frac{m_{C\text{-}xNi-LCCM} - \frac{(100 + W_L) * m_{xNi-LCCM}}{100}}{\frac{N_{Ni} * m_{xNi-LCCM}}{100}} \quad (4)$$

Table 2 presents the carbon yield achieved using the xNi-LCCM catalysts at temperatures of 700 °C, 750 °C, 800 °C, and 850 °C for 15 h, respectively, in pure CH_4. The experiment reveals that no carbon material was produced over xNi-LCCM at 700 °C. It was also found that at all test temperatures, there was no carbon deposition on the 00Ni-LCCM catalyst, meaning the carbon yield was zero. This is consistent with the earlier XRD test results (see Figure 5C).

When the Ni to LCCM molar ratio was 0.2, as in the 02Ni-LCCM sample, the carbon yield reached 0.32 $g_C/g_{02Ni\text{-}LCCM}$ at 750 °C. According to the XRD results mentioned above, after calcination at 1050 °C for 10h in air, all the nickel entered the B-site of LCCM to form $(La_{0.75}Ca_{0.25})(Cr_{0.5}Mn_{0.5}Ni_{0.2})O_{3-\delta}$, and LCCM did not promote the catalytic cracking of methane. Carbon was produced on the 02Ni-LCCM surface, further indicating that under a reducing atmosphere, nickel can exsolve from LCCM and migrate to the surface to become an active catalyst. As listed in Table 2, the carbon yields of 02Ni-LCCM at 800 °C and 850 °C are nearly the same as at 750 °C. This is likely because the active catalyst components exsolve from the internal lattice of 02Ni-LCCM and distribute on the surface of LCCM particles, which are not prone to sintering. However, the carbon yield is too low to have commercial value. Therefore, we are attempting to further increase the content of the nickel oxide promoter.

As summarized in Table 2, at 750 °C, the carbon yield increased with Ni concentration. However, the $Y_{C\text{-}Ni}$ relative to Ni concentration remained nearly constant, between 17.04 to 17.63 g_C/g_{Ni}, when the Ni to LCCM

molar ratio exceeded 1.5. This indicates that higher Ni concentrations were not advantageous due to severe Ni agglomeration and sintering. This phenomenon persisted at elevated temperatures of 800 °C and 850 °C. For instance, using 15Ni-LCCM as an example, an increase in the testing temperature led to a decrease in carbon yield, from 17.04 g_C/g_{Ni} to 10.49 g_C/g_{Ni}, suggesting intensified Ni sintering at elevated temperatures. Therefore, the optimal temperature for maximum carbon yield appears to be 750 °C.

Thermo Gravimetric Analysis (TGA) was performed on carbon nanomaterials produced over the xNi-LCCM series samples using a TGA Q500 instrument. The heating rate was set at 5 °C ·min^{-1} in an airflow of 100 mL·min^{-1}. Figure 6 displays the TGA curves for the carbon nanomaterials produced over xNi-LCCM. Generally, the oxidative stability of carbon nanotubes is influenced by defect sites in graphite walls and nanotube diameters[43]. As evident from Figure 6, the primary weight losses for all carbon products occur between 500 and 700 °C, with the DTG peaks around 600 °C. This indicates that the quality of the carbon products is similar.

Table 3 lists two types of weight loss data. The first type was calculated based on the carbon yield, representing the total weight loss of the obtained carbon nanomaterials, including the reduced sample, and evaluating the overall carbon yield. TGA is another technique for assessing carbon yield. It requires only a 10 mg sample and provides a localized view of the carbon yield. The weight loss figures calculated based on carbon yield closely match the TGA analysis results, implying that the carbon nanomaterials and catalyst samples are homogeneous.

Methane conversion and H_2 production over xNi-LCCM

Figure 7 presents the catalytic thermal decomposition of methane into hydrogen over xNi-LCCM samples in a fixed bed (refer to Figure 3) as a function of time-on-stream at 750 °C, 800 °C, and 850 °C. There are significant differences in the catalytic decomposition activities of methane over these samples at various temperatures. From Figure 7, the following observations can be made: First, the methane conversion rate initially increases with the nickel content, then stabilizes, and the highest conversion rates on the 15Ni-LCCM, 20Ni-LCCM, and 25Ni-LCCM samples are very similar. Second, the active duration for methane cracking catalyzed by the catalyst noticeably increases with the nickel content. Third, the active duration for methane cracking catalysis decreases significantly with rising test temperatures, mainly due to high temperatures promoting sintering of the reduced active catalyst. In summary, the methane conversion rate results from the Gas Chromatography (GC) online test align entirely with the trends in carbon yield results as a function of nickel content and test temperatures.

Microstructure of xNi-LCCM samples and carbon products

Morphology of xNi-LCCM samples

Figure 8 illustrates the morphology of xNi-LCCM samples after being calcined at 1050 °C for ten h in the air to evaluate the microstructural changes due to the calcination process. As shown in Figure 8A, after calcination of 00Ni-LCCM, the particle size is uniformly distributed around 0.5 to 1 mm. For 02Ni-LCCM and 05Ni-LCCM, where the molar ratios of Ni to LCCM are 0.2 and 0.5, respectively, the powder shows obvious signs of sintering and growth. As the molar ratio of Ni to LCCM increases further, the sintering of the powder becomes more severe, as depicted in Figure 8D-G. The FESEM images reveal significant sintering of the catalysts, particularly notable in samples with higher nickel content. This sintering effect manifests as densification and growth of the catalyst particles, which can adversely affect the surface area critical for catalytic activity.

Table 3. Weight loss of carbon produced over xNi-LCCM under CH_4 at 750 °C for 15 h

Sample	Calculated based on carbon yield		TGA analysis	
	Residue/wt.%	Weight loss/wt.%	Residue/wt.%	Weight loss/wt.%
00Ni-LCCM	100.00	0.00	100.08	0.00
02Ni-LCCM	75.75	24.24	76.64	23.36
05Ni-LCCM	44.84	52.20	45.64	54.36
10Ni-LCCM	25.51	74.49	25.87	74.13
15Ni-LCCM	18.45	81.56	19.65	80.35
20Ni-LCCM	15.22	84.78	16.35	83.65
25Ni-LCCM	13.37	86.63	14.86	86.14

LCCM: $(La_{0.75}Ca_{0.25})(Cr_{0.5}Mn_{0.5})O_{3-\delta}$; TGA: A thermogravimetric analyzer.

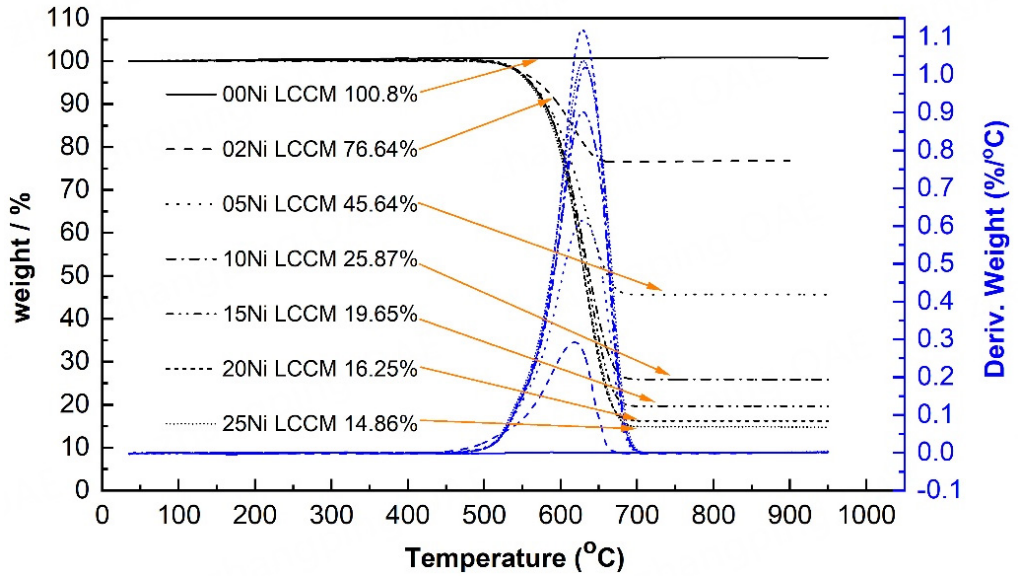

Figure 6. TGA and DTG diagrams for carbon materials deposited on xNi-LCCM at 750 °C under CH_4 for 15 h. TGA: A thermogravimetric analyzer; DTG: Differential thermal gravimetry; LCCM: $(La_{0.75}Ca_{0.25})(Cr_{0.5}Mn_{0.5})O_{3-\delta}$.

The distribution of nickel oxide was particularly pronounced, with excess nickel visibly forming aggregates around the perovskite LCCM particles. This aggregation likely results from the high-temperature conditions during calcination, which facilitate nickel oxide migration and growth around the particle, LCCM, surfaces. The images show that the nickel oxide does not remain evenly distributed but clusters in certain areas.

This uneven distribution and excessive growth of nickel oxide are crucial because they can impact the efficiency of methane decomposition by limiting the available active sites and potentially leading to deactivation of the catalyst through the covering of active sites by nickel aggregates. Additionally, the sintering and aggregation indicate that the thermal stability of the catalyst might be compromised at temperatures required for optimal catalytic activity, which is a vital consideration for scaling up this process for industrial applications.

Morphology of carbon products on xNi-LCCM

Figure 9 illustrates the morphology of carbon nanomaterials deposited over the xNi-LCCM catalysts at 750 °C under methane for 15 h. As shown in Figure 9A, there are no carbon nanomaterials on the LCCM

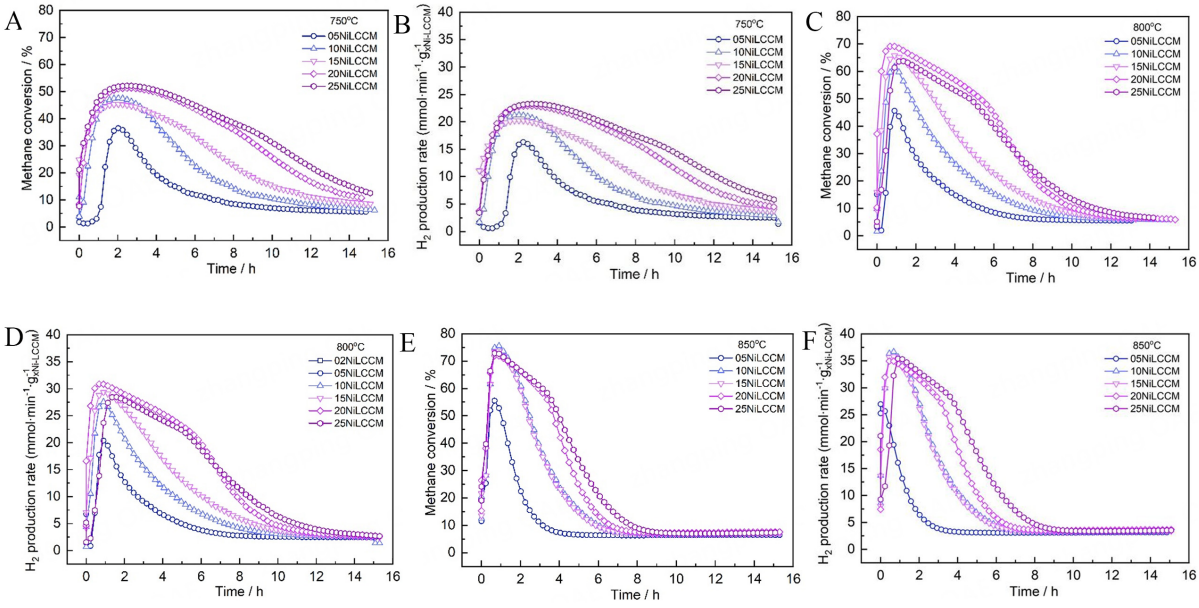

Figure 7. Methane Conversion as a Function of time on stream over xNi-LCCM Samples at (A) 750 °C; (C) 800 °C; and (E) 850 °C; respectively. Profiles of H_2 formation rate as a function of time on stream over xNi-LCCM samples at (B) 750 °C; (D) 800 °C; and (F) 850 °C, respectively. LCCM: $(La_{0.75}Ca_{0.25})(Cr_{0.5}Mn_{0.5})O_{3-\delta}$.

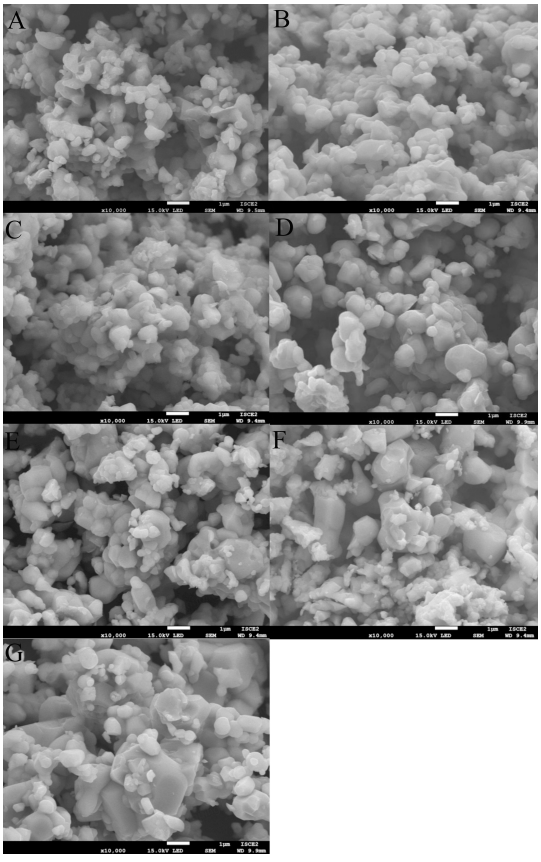

Figure 8. Morphology of xNi-LCCM samples after being calcined at 1000 °C for 10 h in air, (A)00Ni-LCCM; (B) 02Ni-LCCM; (C) 05Ni-LCCM; (D) 10Ni-LCCM; (E) 15Ni-LCCM; (F) 20Ni-LCCM and (G) 25Ni-LCCM. LCCM: $(La_{0.75}Ca_{0.25})(Cr_{0.5}Mn_{0.5})O_{3-\delta}$.

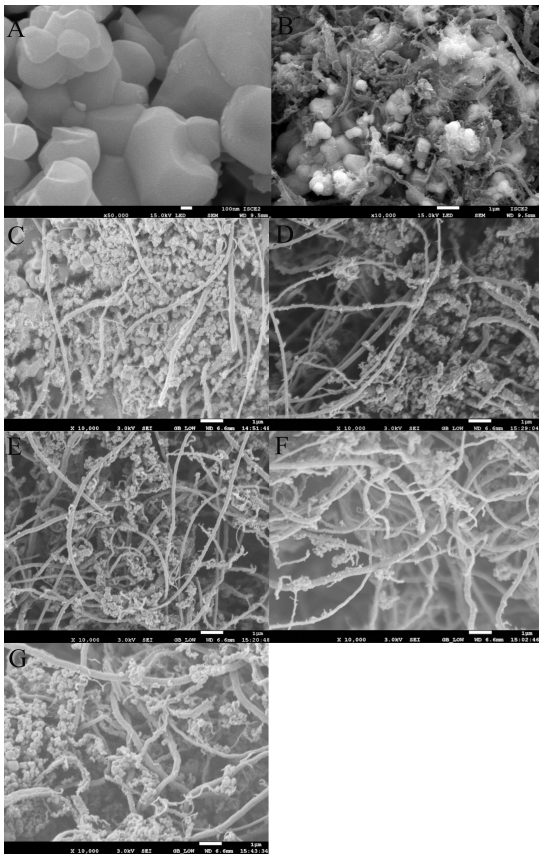

Figure 9. Morphology of carbon materials deposited over (A)00Ni-LCCM; (B) 02Ni-LCCM, (C) 05Ni-LCCM; (D) 10Ni-LCCM; (E) 15Ni-LCCM; (F) 20Ni-LCCM and (G) 25Ni-LCCM at 750 °C under methane atmosphere for 15 h. LCCM: $(La_{0.75}Ca_{0.25})(Cr_{0.5}Mn_{0.5})O_{3-\delta}$.

surface. The results reveal that carbon tubes are the predominant morphological structures observed. Despite the sintering observed in the catalyst base, FESEM images confirmed that the carbon structures remained consistent in both shape and size, indicating that the catalytic sites necessary for carbon formation remain active and accessible even when the nickel content is high. This suggests a resilience in the catalytic functionality concerning carbon material production, which is promising for applications requiring consistent carbon nanomaterial properties. From Figure 9, it is apparent that the diameters of the carbon tubes are relatively consistent, aligned with the findings of the main decomposition temperature of the carbon nanomaterials measured by thermogravimetric analysis in Figure 6.

In summary, while the FESEM analysis highlighted challenges with catalyst stability and nickel distribution, it also reaffirmed the catalyst's ability to facilitate consistent production of carbon nanomaterials under high-temperature conditions. Further optimizations in catalyst formulation and preparation could mitigate sintering effects while maintaining or enhancing the desired catalytic properties.

CONCLUSIONS

This study demonstrated that nickel addition enhances the catalytic performance of LCCM perovskite in methane decomposition, optimizing the production of turquoise hydrogen and carbon nanomaterials. The optimal nickel to LCCM molar ratio was identified as 1.5, balancing catalytic efficiency and material costs and paving the way for future industrial applications. The results show that LCCM can stably exist in both oxidizing and reducing atmospheres, and it exhibits no catalytic activity for methane decomposition under

these conditions. When the molar ratio of nickel to LCCM is 0.2, although Ni can fully enter the B-site of LCCM, the phenomenon of metal exsolution under a reducing atmosphere causes nickel to leach from the B-site of LCCM and accumulate on its surface, thereby becoming a catalyst that promotes the decomposition of methane. According to XRD results, when the nickel to LCCM molar ratio exceeds 0.5, not all nickel can enter the B-site of LCCM, and some of the nickel coexists with LCCM in the form of nickel oxide. FESEM analysis of xNi-LCCM, calcined at 1050 °C for ten h in the air, confirms severe sintering with excess nickel oxide distributed around the LCCM particles. At this point, the nickel leached from the B-site and the free nickel together promote the CDM, co-producing hydrogen and nanocarbon nanomaterials. At an operational temperature of 750 °C, the optimized Ni to LCCM molar ratio of 1.5 produced a peak carbon yield of 17.04 gC/gNi. Further increases in this ratio to 2.0 and 2.5 resulted in slightly higher yields of 17.17 gC/gNi and 17.63 gC/gNi, respectively. These incremental increases indicate a diminishing return on higher nickel content, suggesting an optimal catalyst formulation at a 1.5 molar ratio. The morphology of the carbon nanomaterials is unaffected by the molar ratio of NiO promoter to LCCM and remains nearly the same within the scope of this study.

DECLARATIONS

Authors' contributions

Investigation, methodology, writing-original draft, writing-review and editing: Zhang, L.
Investigation, writing-review and editing: Zhang, W.
Review and editing: Poh, C. K.; Ding, O. L.; Zeng, J.; Cao, G.; Abubakar, S.
Data collection: He, H.; Kouk, Q. Y.
Funding acquisition, supervision, methodology, review: Zhang, L.; Chan, S. H.

Availability of data and materials

Data and materials will be made available upon request by authors.

Financial support and sponsorship

This work was supported by ExxonMobil through its membership in the Singapore Energy Center. This acknowledgment should not be considered an endorsement of the results by ExxonMobil.

Conflicts of interest

All authors declared that there are no conflicts of interest.

Ethical approval and consent to participate

Not applicable.

Consent for publication

Not applicable.

REFERENCES

1. Gaucher, E. C. New perspectives in the industrial exploration for native hydrogen. *Elements* **2020**, *16*, 8-9. DOI
2. Tong, S.; Miao, B.; Zhang, L.; Chan, S. H. Decarbonizing natural gas: a review of catalytic decomposition and carbon formation mechanisms. *Energies* **2022**, *15*, 2573. DOI
3. Tong, S.; Miao, B.; Zhang, W.; Zhang, L.; Chan, S. H. Optimization of methane catalytic decomposition in a fluidized bed reactor: a computational approach. *Energy. Conver. Manag.* **2023**, *297*, 117719. DOI
4. Ighalo, J. O.; Amama, P. B. Recent advances in the catalysis of steam reforming of methane (SRM). *Int. J. Hydrogen. Energy.* **2024**,

51, 688-700. DOI
5. Ambrosetti, M.; Bonincontro, D.; Balzarotti, R.; Beretta, A.; Groppi, G.; Tronconi, E. H_2 production by methane steam reforming over Rh/Al_2O_3 catalyst packed in Cu foams: a strategy for the kinetic investigation in concentrated conditions. *Catal. Today.* **2022**, *387*, 107-18. DOI
6. Nnabuife, S. G.; Ugbeh-johnson, J.; Okeke, N. E.; Ogbonnaya, C. Present and projected developments in hydrogen production: a technological review*. *Carbon. Capture. Sci. Technol.* **2022**, *3*, 100042. DOI
7. Navas-Anguita, Z.; García-Gusano, D.; Dufour, J.; Iribarren, D. Revisiting the role of steam methane reforming with CO_2 capture and storage for long-term hydrogen production. *Sci. Total. Environ.* **2021**, *771*, 145432. DOI PubMed
8. Korányi, T. I.; Németh, M.; Beck, A.; Horváth, A. Recent advances in methane pyrolysis: turquoise hydrogen with solid carbon production. *Energies* **2022**, *15*, 6342. DOI
9. Ingale, G. U.; Kwon, H.; Jeong, S.; et al. Assessment of greenhouse gas emissions from hydrogen production processes: turquoise hydrogen vs. steam methane reforming. *Energies* **2022**, *15*, 8679. DOI
10. Chan, S. H.; Ding, O. L.; Hoang, D. L. A Thermodynamic view of partial oxidation, steam reforming, and autothermal reforming on methane. *Int. J. Green. Energy.* **2004**, *1*, 265-78. DOI
11. Hoang, D.; Chan, S.; Ding, O. Kinetic and modelling study of methane steam reforming over sulfide nickel catalyst on a gamma alumina support. *Chem. Eng. J.* **2005**, *112*, 1-11. DOI
12. Hoang, D.; Chan, S.; Ding, O. Hydrogen production for fuel cells by autothermal reforming of methane over sulfide nickel catalyst on a gamma alumina support. *J. Power. Sources.* **2006**, *159*, 1248-57. DOI
13. Matin, N. S.; Flanagan, W. P. Environmental performance of nonthermal plasma dry and conventional steam reforming of methane for hydrogen production: application of life cycle assessment methodology. *Int. J. Hydrogen. Energy.* **2024**, *49*, 1405-13. DOI
14. Ding, X.; Li, B.; Yang, Y.; Liu, X.; Guo, Y.; Wang, Y. Steam reforming of methane over nickel-aluminum spinel-derived catalyst. *Int. J. Hydrogen. Energy.* **2024**, *51*, 1256-66. DOI
15. Do, T. N.; Kwon, H.; Park, M.; Kim, C.; Kim, Y. T.; Kim, J. Carbon-neutral hydrogen production from natural gas via electrified steam reforming: techno-economic-environmental perspective. *Energy. Convers. Manag.* **2023**, *279*, 116758. DOI
16. Hamdan, M.; Halawy, L.; Abdel, K. A. N.; Ahmad, M. N.; Zeaiter, J. Analytical review of the catalytic cracking of methane. *Fuel* **2022**, *324*, 124455. DOI
17. Qian, J. X.; Chen, T. W.; Enakonda, L. R.; et al. Methane decomposition to produce CO -free hydrogen and nano-carbon over metal catalysts: a review. *Int. J. Hydrogen. Energy.* **2020**, *45*, 7981-8001. DOI
18. Qian, J.; Li, H.; Sun, D.; et al. Tuning Mg-Fe-O solid solutions towards optimized exsolution of active sites for thermal catalytic decomposition of methane. *Chem. Eng. J.* **2024**, *497*, 154595. DOI
19. Abbas, H. F.; Wan, D. W. Hydrogen production by methane decomposition: a review. *Int. J. Hydrogen. Energy.* **2010**, *35*, 1160-90. DOI
20. Hazra, M.; Croiset, E.; Hudgins, R. R.; Silveston, P. L.; Elkamel, A. Experimental investigation of the catalytic cracking of methane over a supported Ni catalyst. *Can. J. Chem. Eng.* **2009**, *87*, 99-105. DOI
21. Mcconnachie, M.; Konarova, M.; Smart, S. Literature review of the catalytic pyrolysis of methane for hydrogen and carbon production. *Int. J. Hydrogen. Energy.* **2023**, *48*, 25660-82. DOI
22. Abánades, A.; Rubbia, C.; Salmieri, D. Thermal cracking of methane into hydrogen for a CO_2-free utilization of natural gas. *Int. J. Hydrogen. Energy.* **2013**, *38*, 8491-6. DOI
23. Jin, L.; Si, H.; Zhang, J.; et al. Preparation of activated carbon supported $Fe-Al_2O_3$ catalyst and its application for hydrogen production by catalytic methane decomposition. *Int. J. Hydrogen. Energy.* **2013**, *38*, 10373-80. DOI
24. Amin, A. M.; Croiset, E.; Epling, W. Review of methane catalytic cracking for hydrogen production. *Int. J. Hydrogen. Energy.* **2011**, *36*, 2904-35. DOI
25. Ashik, U.; Wan, D. W.; Abbas, H. F. Production of greenhouse gas free hydrogen by thermocatalytic decomposition of methane - a review. *Renew. Sustain. Energy. Rev.* **2015**, *44*, 221-56. DOI
26. Maneerung, T.; Hidajat, K.; Kawi, S. $LaNiO_3$ perovskite catalyst precursor for rapid decomposition of methane: influence of temperature and presence of H_2 in feed stream. *Catalysis. Today.* **2011**, *171*, 24-35. DOI
27. Takenaka, S.; Shigeta, Y.; Tanabe, E.; Otsuka, K. Methane decomposition into hydrogen and carbon nanofibers over supported Pd-Ni catalysts. *J. Catal.* **2003**, *220*, 468-77. DOI
28. Gallego G, Barrault J, Batiot-dupeyrat C, Mondragón F. Production of hydrogen and MWCNTs by methane decomposition over catalysts originated from $LaNiO_3$ perovskite. *Catal. Today.* **2010**, *149*, 365-71. DOI
29. Jiang, S.; Chen, X.; Chan, S.; Kwok, J.; Khor, K. $(La_{0.75}Sr_{0.25})(Cr_{0.5}Mn_{0.5})O_3$/YSZ composite anodes for methane oxidation reaction in solid oxide fuel cells. *Solid. State. Ionics.* **2006**, *177*, 149-57. DOI
30. Jiang, S. P.; Chen, X. J.; Chan, S. H.; Kwok, J. T. GDC-impregnated $(La_{0.75}Sr_{0.25})(Cr_{0.5}Mn_{0.5})O_3$ anodes for direct utilization of methane in solid oxide fuel cells. *J. Electrochem. Soc.* **2006**, *153*, A850. DOI
31. Sfeir, J.; Buffat, P. A.; Möckli, P.; et al. Lanthanum chromite based catalysts for oxidation of methane directly on SOFC anodes. *J. Catal.* **2001**, *202*, 229-44. DOI
32. Chen, X.; Liu, Q.; Khor, K.; Chan, S. High-performance $(La,Sr)(Cr,Mn)O_3$/$(Gd,Ce)O_{2-\delta}$ composite anode for direct oxidation of methane. *J. Power. Sources.* **2007**, *165*, 34-40. DOI
33. Jiang, S. P.; Zhang, L.; Zhang, Y. Lanthanum strontium manganese chromite cathode and anode synthesized by gel-casting for solid

oxide fuel cells. *J. Mater. Chem.* **2007**, *17*, 2627. DOI

34. Li, H.; Sun, G.; Xie, K.; et al. Chromate cathode decorated with in-situ growth of copper nanocatalyst for high temperature carbon dioxide electrolysis. *Int. J. Hydrogen. Energy.* **2014**, *39*, 20888-97. DOI
35. Sun, H.; He, X.; Huang, X.; Gan, L. Modification of LSCM structure by anchoring alloy nanoparticles for efficient CO_2 electrolysis. *Energy. Fuels.* **2024**, *38*, 3436-44. DOI
36. Jardiel, T.; Caldes, M.; Moser, F.; Hamon, J.; Gauthier, G.; Joubert, O. New SOFC electrode materials: the Ni-substituted LSCM-based compounds $(La_{0.75}Sr_{0.25})(Cr_{0.5}Mn_{0.5-x}Nix)O_{3-\delta}$ and $(La_{0.75}Sr_{0.25})(Cr_{0.5-x}NixMn_{0.5})O_{3-\delta}$. *Solid. State. Ionics.* **2010**, *181*, 894-901. DOI
37. Carrillo, A. J.; López-García, A.; Delgado-Galicia, B.; Serra, J. M. New trends in nanoparticle exsolution. *Chem. Commun.* **2024**, *60*, 7987-8007. DOI PubMed
38. Zhang, L.; Ping, J. S.; Siang, C. C.; Zhang, Y. Synthesis and performance of $(La_{0.75}Sr_{0.25})_{1-x}(Cr_{0.5}Mn_{0.5})O_3$ cathode powders of solid oxide fuel cells by gel-casting technique. *J. Electrochem. Soc.* **2007**, *154*, B577. DOI
39. Zhang, L.; Chen, X.; Jiang, S. P.; He, H. Q.; Xiang, Y. Characterization of doped $La_{0.7}A_{0.3}Cr_{0.5}Mn_{0.5}O_{3-\delta}$ (A=Ca, Sr, Ba) electrodes for solid oxide fuel cells. *Solid. State. Ionics.* **2009**, *180*, 1076-82. DOI
40. Jiang, S. P.; Zhang, L.; He, H. Q.; Yap, R. K.; Xiang, Y. Synthesis and characterization of lanthanum silicate apatite by gel-casting route as electrolytes for solid oxide fuel cells. *J. Power. Sources.* **2009**, *189*, 972-81. DOI
41. Maneerung, T.; Hidajat, K.; Kawi, S. Co-production of hydrogen and carbon nanofibers from catalytic decomposition of methane over $LaNi_{(1-x)}M_x O_{3-\alpha}$ perovskite (where M=Co, Fe and X=0, 0.2, 0.5, 0.8, 1). *Int. J. Hydrogen. Energy.* **2015**, *40*, 13399-411. DOI
42. Duma, Z. G.; Swartbooi, A.; Musyoka, N. M. Thermocatalytic decomposition of methane to low-carbon hydrogen using $LaNi_{1-x}Cu_xO_3$ perovskite catalysts. *Appl. Catal. A:. Gen.* **2024**, *677*, 119703. DOI
43. Awadallah, A.; Aboul-enein, A.; El-desouki, D.; Aboul-gheit, A. Catalytic thermal decomposition of methane to CO*x*-free hydrogen and carbon nanotubes over MgO supported bimetallic group VIII catalysts. *Appl. Surf. Sci.* **2014**, *296*, 100-7. DOI